

Two-dimensional topological quantum walks in the momentum space of structured light

Alessio D’Errico,^{1,*} Filippo Cardano,^{1,†} Maria Maffei,^{1,2} Alexandre Dauphin,^{2,‡} Raouf Barboza,¹ Chiara Esposito,¹ Bruno Piccirillo,¹ Maciej Lewenstein,^{2,3} Pietro Massignan,^{2,4,§} and Lorenzo Marrucci^{1,5}

¹*Dipartimento di Fisica, Università di Napoli Federico II,
Complesso Universitario di Monte Sant’Angelo, Via Cintia, 80126 Napoli, Italy*

²*ICFO – Institut de Ciències Fotoniques, The Barcelona Institute
of Science and Technology, 08860 Castelldefels (Barcelona), Spain*

³*ICREA – Institució Catalana de Recerca i Estudis Avançats,
Pg. Lluís Companys 23, 08010 Barcelona, Spain*

⁴*Departament de Física, Universitat Politècnica de Catalunya, Campus Nord B4-B5, 08034 Barcelona, Spain*

⁵*CNR-ISASI, Institute of Applied Science and Intelligent Systems,
Via Campi Flegrei 34, 80078 Pozzuoli (NA), Italy*

Quantum walks are powerful tools for building quantum algorithms, modeling transport phenomena, and designing topological systems. Here we present a photonic implementation of a quantum walk in two spatial dimensions, where the lattice of walker positions is encoded in the transverse-wavevector components of a paraxial light beam. The desired quantum dynamics is obtained by means of a sequence of liquid-crystal devices (“*g*-plates”), which apply polarization-dependent transverse kicks to the photons in the beam. We first characterize our setup, and then benchmark it by implementing a periodically-driven Chern insulator and probing its topological features. Our platform is compact, versatile and cost-effective: most evolution parameters are controlled dynamically, the walker distribution is detected in a single shot, and the input state can be tailored at will. These features offer exciting prospects for the photonic simulation of two-dimensional quantum systems.

I. INTRODUCTION

Quantum walks (QWs) are the quantum counterparts of classical random walks, and describe particles (walkers) whose discrete dynamics is conditioned by the instantaneous configuration of their spin-like degree of freedom (the coin) [1]. QWs are ideal candidates for implementing quantum search algorithms and universal quantum computation [2, 3], and have been used to model energy transport in photosynthetic processes [4]. These systems bear close analogies with electrons in periodic potentials, and it was shown that QWs can host all possible symmetry-protected topological phases displayed by non-interacting fermions in one or two spatial dimensions (1D or 2D) [5]. Practical implementations of quantum walks have been demonstrated, for instance, with ultracold atoms in optical lattices [6–9], superconducting circuits [10] and photonic systems [11–16].

In optical architectures, the lattice coordinates have been encoded in different degrees of freedom of light, such as the arrival time of a pulse at a detector [14, 17, 18], the optical path of the beam [11–13, 19, 20], or the orbital angular momentum [15]. The coin is typically encoded in the polarization degree of freedom or in the entrance port of beam splitters. In a remarkable series of experiments, QWs proved instrumental in studying the evolution of correlated photons [12, 13], the effects

of decoherence [11, 17] and interactions [14], Anderson localization [21], quantum transport in presence of disorder [22], and topological phenomena of Floquet systems [10, 19, 23–28]. Despite being so fruitful, experimental research on QWs has been almost entirely focused on 1D systems. Few exceptions are the studies presented in Refs. [14, 18, 29], where a 2D walk was cleverly simulated by folding a 2D lattice in a 1D chain, and in Ref. [30], where path and OAM encoding were combined. Very recently, a continuous-time walk has been realized in a 2D array of coupled-waveguides [31, 32].

Here, we report the experimental realization of a discrete-time quantum walk in 2D based on encoding the walker position in the transverse wavevector (or photon momentum), which is an inherently 2D degree of freedom. Unlike the common approach of using distinct optical paths (as in parallel waveguides), in our system the photonic evolution takes place within a single light beam that acquires a complex internal structure as it propagates. The core of our photonic QW simulator is a stack of closely-spaced liquid-crystal devices, conceptually similar to standard *g*-plates [33]. We present a proof-of-principle demonstration of our platform by generating up to 5 steps of a 2D QW, with both localized and extended initial inputs [18, 34, 35].

Quite remarkably, the unitary evolution of our QW actually realizes a periodically-driven (Floquet) Chern insulator. To characterize this system, we first probe the energy dispersion of one of the bands of the effective Hamiltonian by tracking the free displacement of a wavepacket. Then we probe the Berry curvature of the band by repeating the tracking under the action of a constant force. Upon sampling uniformly across the whole

* AD’E and FC contributed equally to this work

† filippo.cardano2@unina.it

‡ alexandre.dauphin@icfo.eu

§ pietro.massignan@upc.edu

band, the average transverse displacement provides us a straightforward and accurate measurement of the Chern number of that band.

II. RESULTS

A. Quantum walks in the transverse wavevector of light

A discrete-time QW on a square lattice in 2D results from the repeated action of a unitary operator U on a quantum system, the walker, and its internal spin-like degree of freedom, the coin [36]. After t discrete steps, a given initial state $|\Psi_0\rangle$ evolves according to $|\Psi(t)\rangle = U^t|\Psi_0\rangle$. The step operator U typically includes a spin rotation W , and discrete displacements of the walker along the directions x and y , generated by spin-dependent translation operators T_x and T_y . In the simplest case, the Hilbert space of the coin has dimension two [5, 34, 37]. In our photonic QW implementation, we encode the coin into light polarization. For definiteness, we use left and right circular polarizations ($|L\rangle, |R\rangle$) as the basis states (with handedness defined from the point of view of the receiver), like in our earlier realization of a QW with twisted light [15].

The main novelty of the setup considered here lies in encoding the discrete dimensionless coordinate of the walker $\mathbf{m} = (m_x, m_y)$ on a 2D square lattice in the transverse momentum of light. In particular, we use Gaussian modes whose mean transverse wavevector assumes the discrete values $\mathbf{k}_\perp = \Delta k_\perp \mathbf{m}$. The lattice constant Δk_\perp is taken to be much smaller than the longitudinal wavevector component $k_z \approx 2\pi/\lambda$ (where λ is the light wavelength), so that these modes propagate along a direction that is only slightly tilted with respect to the z axis. More explicitly, a generic light mode in our setup reads:

$$|\mathbf{m}, \phi\rangle = A(x, y, z) e^{i[\Delta k_\perp (m_x x + m_y y) + k_z z]} \otimes |\phi\rangle, \quad (1)$$

where $A(x, y, z)$ is a Gaussian envelope with large beam radius w_0 in the transverse xy plane and $|\phi\rangle$ denotes the polarization state (see [Supplementary Note 1](#) for more details). Accordingly, arbitrary superpositions of these modes still form a single optical beam, travelling approximately along the z axis. Only in the far field, or equivalently in the focal plane of a lens, these modes become spatially separated and their relative distribution can be easily read-out (see Figs. [1a,b](#)). The parameters w_0 and Δk_\perp are chosen so that these modes almost perfectly overlap spatially while propagating in the whole QW apparatus (as long as $|m_x|$ and $|m_y|$ are not too large), and have negligible crosstalk in the lens focal plane.

The QW dynamics is implemented with the apparatus depicted schematically in Fig. [1a](#), and described in greater detail in [Supplementary Note 2](#). A collimated Gaussian laser beam passes through a sequence of closely-spaced liquid crystal (LC) plates which realize

both walker-translation and coin-rotation operators. At the exit of the walk, a camera placed in the focal plane of a lens reads out the field intensity, providing the coordinates distribution of the walker (as in Fig. [1b](#); see also [Supplementary Note 3](#)). If needed, also the polarization components may be straightforwardly read out (see [Supplementary Fig. S2](#)).

The elements yielding the QW dynamics are optical devices consisting of thin layers of LC sandwiched between glass plates. The local orientation $\alpha(x, y)$ of the LC optic axis in the plane of the plate can follow arbitrary patterns, imprinted during the fabrication by a photo-alignment technique. The birefringent optical retardation δ of the LC may instead be controlled dynamically through an external electric field [38]. Such plates give rise to coin rotations or walker translations, depending on the optic axis pattern. For example, a spin-dependent translation operator in the x direction is obtained when the local orientation α increases linearly along x :

$$\alpha(x, y) = \pi x/\Lambda + \alpha_0, \quad (2)$$

where Λ is the spatial periodicity of the angular pattern and α_0 is a constant (see Fig. [1c](#)). This patterned birefringent structure is also known as a “polarization grating”, and hence we refer here to these devices as “ g -plates” (as opposed to the q -plates used in our previous works, which have azimuthally-varying patterns [33]). In the basis of circular polarizations $|L\rangle = (1, 0)^T$ and $|R\rangle = (0, 1)^T$, this g -plate acts as follows (see Methods and [Supplementary Note 4](#) for a complete derivation):

$$T_x \equiv \begin{pmatrix} \cos(\delta/2) & i \sin(\delta/2) e^{-2i\alpha_0} \hat{t}_x \\ i \sin(\delta/2) e^{2i\alpha_0} \hat{t}_x^\dagger & \cos(\delta/2) \end{pmatrix}, \quad (3)$$

where \hat{t}_x and \hat{t}_x^\dagger are the (spin-independent) left and right translation operators along x , acting respectively as $\hat{t}_x|m_x, m_y, \phi\rangle = |m_x - 1, m_y, \phi\rangle$ and $\hat{t}_x^\dagger|m_x, m_y, \phi\rangle = |m_x + 1, m_y, \phi\rangle$. The spatial periodicity Λ of the LC pattern controls the momentum lattice spacing $\Delta k_\perp = 2\pi/\Lambda$. It is sufficient to set $\Lambda \sim w_0$ to avoid mode crosstalk. The T_y operator is implemented analogously, imposing a gradient of the LC angle α along y . Finally, the spin rotations W are realized with uniform LC plates acting as standard quarter-wave plates, that is with constant $\alpha = 0$ and $\delta = \pi/2$. In the basis of circular polarizations, this operator acts as

$$W = \frac{1}{\sqrt{2}} \begin{pmatrix} 1 & i \\ i & 1 \end{pmatrix}. \quad (4)$$

B. A 2D quantum walk

To benchmark our photonic platform, we implement five complete steps of a discrete-time 2D quantum walk, generated by the unit step operator

$$U = T_y T_x W, \quad (5)$$

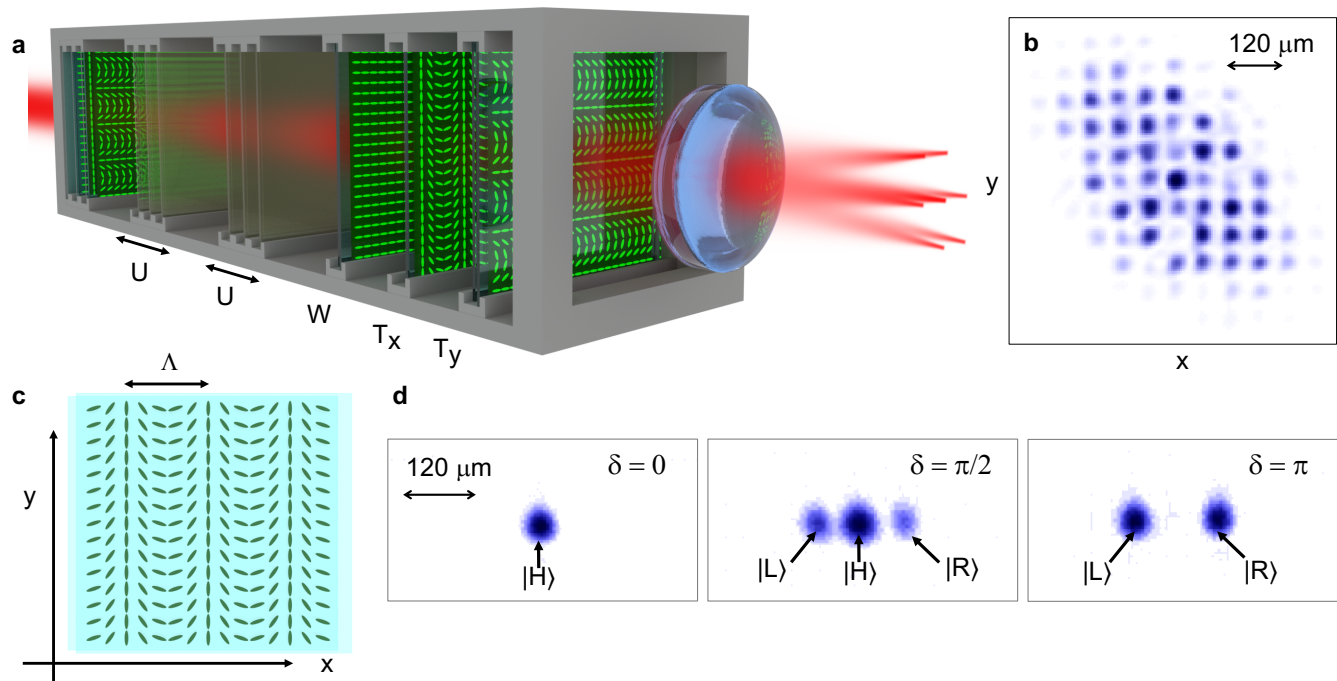


FIG. 1. **Experimental concept and apparatus.** **a**, A collimated beam crosses a sequence of liquid crystal (LC) devices. Different LC patterns implement coin rotations (W) and spin-dependent walker discrete translations (T_x and T_y). Each evolution step $U = T_y T_x W$ is realized with three LC devices. The walker position is encoded in the transverse momentum of photons, so that walker steps physically correspond to transverse kicks which tilt slightly the photon propagation direction. The transverse diffraction of light remains negligible across the whole set-up, and the entire evolution effectively occurs in a single beam. At the exit of the walk, a lens (with focal distance equal to 50 cm) Fourier-transforms transverse momentum into position, allowing us to resolve and measure individual modes. **b**, The recorded intensity pattern is a regular grid of small Gaussian spots, whose intensities are proportional to the walker's spatial probability distribution. We set the modes beam radius to $w_0 = 5$ mm, that corresponds to a spot size of $\simeq 20 \mu\text{m}$ (radius) on the camera plane. **c**, LC optic-axis pattern for a g -plate which realizes a T_x operator. The spatial period Λ fixes the transverse momentum lattice spacing $\Delta k_\perp = 2\pi/\Lambda$. We use $\Lambda = 5$ mm, so that $\Delta k_\perp = 1.26 \text{ mm}^{-1}$, corresponding to a spacing between spots of $\simeq 63 \mu\text{m}$ on the camera. **d**, Action of a single g -plate T_x on a linearly polarized beam $|\Psi_0\rangle = |0, 0, H\rangle$, where $|H\rangle = (|L\rangle + |R\rangle)\sqrt{2}$, for three different values of δ .

with T_x and T_y tuned at the same value of δ . This evolution represents a generalization of the alternated protocol introduced in Ref. [34].

We start with a localized walker state $|\mathbf{m} = (0, 0), \phi\rangle$, which physically corresponds to a wide input Gaussian beam with radius $w_0 = 5$ mm, propagating along the z direction. In Fig. 2 we show representative data for $\delta = \pi/2$ and a linearly polarized input. The walker distribution remains concentrated along the diagonal $m_x = -m_y$ during the whole evolution, as a consequence of the absence of coin rotation operations between every action of T_x and T_y . All data show an excellent agreement with numerical simulations. A quantitative comparison is provided by computing the similarity $S = (\sum_{\mathbf{m}} \sqrt{P_e P_s})^2 / (\sum_{\mathbf{m}} P_e \sum_{\mathbf{m}} P_s)$ between simulated (P_s) and experimental (P_e) distributions. For the data shown in Fig. 2, we have $S = (98.2 \pm 0.5)\%$, $(98.0 \pm 0.3)\%$, $(98.0 \pm 0.2)\%$ for the distributions at $t = 0, 3, 5$, respectively. The uncertainties on these values are the standard errors of the mean, obtained by repeating each

experiment four times. Distributions obtained for other choices of the coin input state are reported in Supplementary Figs. S5, S6.

C. Quasi-momentum, quasi-energy bands and group velocity

A quantum walk can be regarded as the stroboscopic evolution generated by the (dimensionless) effective Floquet Hamiltonian $H_{\text{eff}} \equiv i \ln U$. The eigenvalues of H_{eff} are therefore defined only up to integer multiples of 2π , and are termed quasi-energies. Both U and H_{eff} admit a convenient representation in the reciprocal space \mathbf{q} associated with the coordinate \mathbf{m} of the walker. As discussed above, the dimensionless coordinate $\mathbf{m} = \mathbf{k}_\perp / \Delta k_\perp$ is encoded in our setup in the transverse momentum \mathbf{k}_\perp of the propagating beam. As such, its conjugate variable corresponds physically to the position vector \mathbf{r}_\perp in the xy transverse plane. We introduce therefore the di-

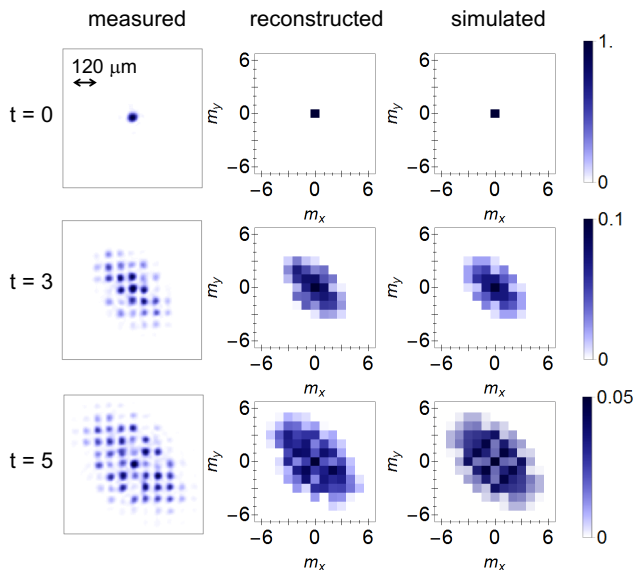


FIG. 2. **2D Quantum Walk on a square lattice.** Spatial probability distributions for a quantum walk with initial condition $|0, 0, H\rangle$ and optical retardation $\delta = \pi/2$. From top to bottom, we display results after 0, 3, and 5 evolution steps. Datapoints are averages of four independent measures.

dimensionless quasi-momentum $\mathbf{q} = -2\pi\mathbf{r}_\perp/\Lambda$, belonging to the square Brillouin zone $[-\pi, \pi]^2$, as the conjugate variable to the walker position \mathbf{m} . The negative sign in the definition of \mathbf{q} provides the standard representation for plane waves $\langle \mathbf{m} | \mathbf{q} \rangle \propto e^{i\mathbf{m}\cdot\mathbf{q}}$. In the space of quasi-momenta the effective Hamiltonian assumes the diagonal form $H_{\text{eff}}(\mathbf{q}) = \varepsilon(\mathbf{q})\mathbf{n}(\mathbf{q}) \cdot \boldsymbol{\sigma}$. Here $\mathbf{n}(\mathbf{q})$ is a unit vector, $\boldsymbol{\sigma} = (\sigma_x, \sigma_y, \sigma_z)$ denotes the three Pauli matrices, and $\varepsilon(\mathbf{q})$ yields the quasi-energies of two bands (as shown in Fig. 3a). In the following, we will denote the complete eigenstates of the system by $|\mathbf{q}, \phi_\pm(\mathbf{q})\rangle$, where \pm refers to the upper/lower band.

In our experiment, we can directly explore the band structure of the system by observing the propagation of walker wavepackets $|\Psi_g(\mathbf{q}_0, \pm)\rangle$ that are sharply peaked around a given quasi-momentum \mathbf{q}_0 and belong to the upper/lower band. These wavepackets are physically generated as narrow Gaussian light beams (with beam radius $w_g \ll \Lambda$) propagating along the direction z , centered around a specific transverse position $\mathbf{r}_{\perp 0} = -\mathbf{q}_0\Lambda/(2\pi)$ at the input port of the QW, and with polarization $|\phi_\pm(\mathbf{q}_0)\rangle$ (see [Supplementary Note 1](#) for details). In the experiment, the choice of transverse position $\mathbf{r}_{\perp 0}$ is easily controlled by translating the whole QW set-up (which is mounted on a single motorized mechanical holder) relative to the input laser beam. Having narrow Gaussian envelopes in the conjugate space \mathbf{q} , these wavepackets are relatively broad Gaussians in the space of walker coordinates \mathbf{m} . They are (approximate) eigenstates of the system, and therefore preserve their shape during propagation. Their center of mass $\langle \mathbf{m} \rangle_{\Psi_g}$ obeys a dynamics

which semi-classically is governed by the group velocity $\mathbf{v}^{(\pm)}(\mathbf{q}_0) = \pm \nabla_{\mathbf{q}} \varepsilon(\mathbf{q})|_{\mathbf{q}=\mathbf{q}_0}$ [15], as shown for instance in Fig. 3b. To measure experimentally the group velocity $\mathbf{v}^{(\pm)}(\mathbf{q}_0)$ we inject a wavepacket $|\Psi_g(\mathbf{q}_0, \pm)\rangle$ in our QW, we detect its average displacement $\Delta\mathbf{m}$ as a function of time-step t , and finally we perform a linear best fit on the displacements versus time (see Fig. 3c). Figure 3d shows a complete mapping of the x component of the upper band's velocity $\mathbf{v}^{(+)}$ for $\delta = \pi/2$. Correspondingly measured values of the y component of $\mathbf{v}^{(+)}$ are reported in [Supplementary Fig. S7](#).

D. Measurement of the Chern number through the anomalous velocity

The energy bands of the effective Hamiltonian generally possess non-zero Berry curvatures. For a 2×2 Hamiltonian like ours, the latter may be written as [39]

$$\Omega_{xy}^{(\pm)}(\mathbf{q}) = \pm \frac{1}{2} \mathbf{n}(\mathbf{q}) \cdot \left[\frac{\partial \mathbf{n}}{\partial q_x} \times \frac{\partial \mathbf{n}}{\partial q_y} \right], \quad (6)$$

The integral of the Berry curvature over the whole Brillouin zone (BZ) gives the Chern number:

$$\nu^{(\pm)} = \int_{\text{BZ}} \frac{d^2\mathbf{q}}{2\pi} \Omega_{xy}^{(\pm)}(\mathbf{q}). \quad (7)$$

The Chern number $\nu^{(\pm)}$ of our QW depends on the optical retardation of our plates. By tuning δ , we can thus switch from a trivial to a topological Chern insulator, as shown for example in Fig. 4a. The complete topological classification of this Floquet system is discussed in [Supplementary Note 5](#).

When a constant unidirectional force is acting on the system, the Berry curvature contributes to the wavepacket displacement in a direction orthogonal to the force (as in the quantum Hall effect). Let us for definiteness consider a force F_x acting along x . Within the adiabatic approximation, the semi-classical equations of motion predict that a wavepacket $|\Psi_g(\mathbf{q}_0, \pm)\rangle$ will experience after a time t a transverse displacement along y given by [40, 41]

$$\Delta m_y = \int_0^t d\tau \left[v_y^{(\pm)}(\mathbf{q}_\tau) + F_x \Omega_{xy}^{(\pm)}(\mathbf{q}_\tau) \right], \quad (8)$$

with $\mathbf{q}_\tau = (q_{0,x} + F_x\tau, q_{0,y})$. The contribution to the velocity coming from the Berry curvature is called anomalous velocity. This result is derived in the adiabatic regime, where the (dimensionless) force is much smaller than the band-gaps of the effective energy, so that inter-band transitions can be neglected. When we consider the overall transverse displacement of a filled band, namely when we integrate Eq. (8) over the whole Brillouin zone, the group-velocity term averages to zero, while the anomalous contributions add up to the band's

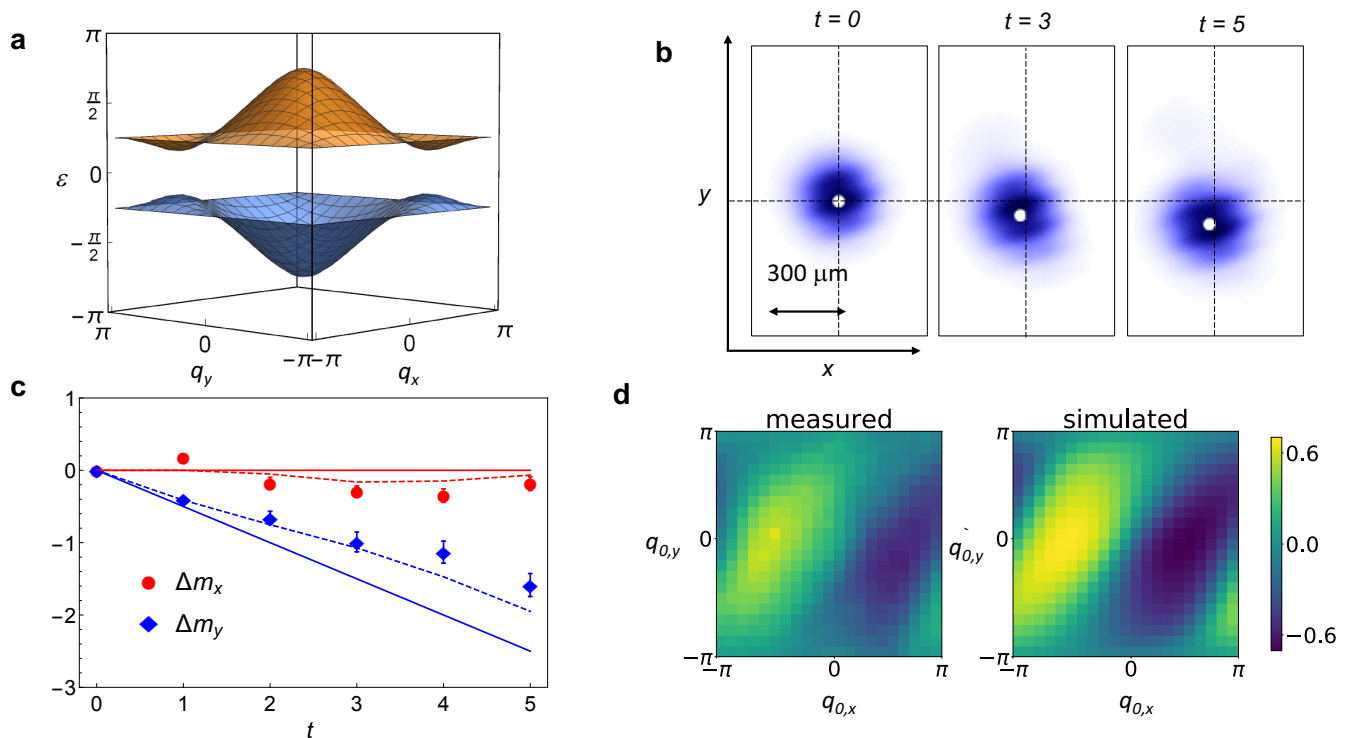


FIG. 3. **Detection of the group velocity at $\delta = \pi/2$.** **a**, Spectrum of the effective Hamiltonian H_{eff} . **b**, Light intensity distribution measured for a wavepacket with $\mathbf{q}_0 = (\pi/2, \pi)$ in the upper band, where the expected group velocity is $\mathbf{v}^{(+)} = (0, -0.5)$. The white marker indicates the center of mass of the wavepacket. The radius w_g of the input beam is (0.62 ± 0.02) mm. In the camera plane, we measure a beam diameter of (0.32 ± 0.01) mm, corresponding to ≈ 5 lattice sites. **c**, Displacement of the wavepacket center of mass, extracted from images as in panel **b**. Experimental results (datapoints) are compared to semiclassical predictions of uniform motion (straight continuous lines), and to complete numerical simulations (dashed lines). Statistical uncertainties include estimated misalignment effects, as discussed in the Methods. **d**, Experimental mapping of the upper band’s group velocity $\mathbf{v}^{(+)}$ along x across the whole Brillouin zone, compared to a complete numerical simulation. Each datapoint is obtained from a linear fit of the center-of-mass displacement of a Gaussian wavepacket in 5 steps.

Chern number [41, 42] (see the Methods and [Supplementary Note 4](#) for details):

$$\langle \Delta m_y \rangle^{(\pm)} \approx \frac{F_x \nu^{(\pm)}}{2\pi} t. \quad (9)$$

To implement a constant force in our set-up, we impose at each step a quasi-momentum variation, which physically corresponds to a transverse spatial displacement of the light beam between each plate. Rather than displacing the beam, it is equivalent (and much simpler) to displace the reference system and the setup in the opposite direction. More specifically, we shift the g -plate acting at time-step t along the x axis by an amount $\Delta x_t = t F_x \Lambda / (2\pi)$ (see the Methods for further details). Then, we sum up the measured displacements Δm_y obtained for 11×11 distinct wave-packets $|\Psi_g(\mathbf{q}_0, -)\rangle$, which provides a homogeneous sampling of the lower band across the whole Brillouin zone and realizes a good approximation of the continuous integral yielding $\langle \Delta m_y \rangle^{(-)}$. Figure 4**b** shows the mean displacement of wavepackets prepared in the lowest energy band for a QW with $\delta = \pi/2$, corresponding to Chern number $\nu^{(-)} = 1$. The

energy bandgap ≈ 1 (see Fig. 4**a**) is sufficiently larger than the applied force $F_x = \pi/20$, thereby ensuring the validity of the adiabatic approximation. Experimental data (empty markers) are compared to the overall band displacement predicted by the semi-classical theory within adiabatic regime (continuous lines), namely $\langle \Delta m_y(t) \rangle^{(-)} = t \nu^{(-)} F_x / (2\pi)$, $\langle \Delta m_x(t) \rangle^{(-)} = 0$. While $\langle \Delta m_y \rangle^{(-)}$ follows the expected curve quite reasonably, the overall $\langle \Delta m_x \rangle^{(-)}$ is found to be not negligible.

To get rid of this spurious contribution, which arises mainly from residual group-velocity effects, we consider also the “inverse protocol” generated by the step operator $U^{-1} = W^{-1} T_x^{-1} T_y^{-1}$. The bands of U^{-1} have the same dispersion as the bands of U , but feature opposite Chern numbers. In this way, if filling the same band, we expect to observe identical contributions from the group velocity dispersion, while the anomalous displacement should be inverted. The step operator U^{-1} can be easily implemented by swapping the T_y and W operators, and changing suitably their retardation (see the Methods and Supplementary Fig. S2). In Fig. 4**b** we show with filled markers the difference (divided by

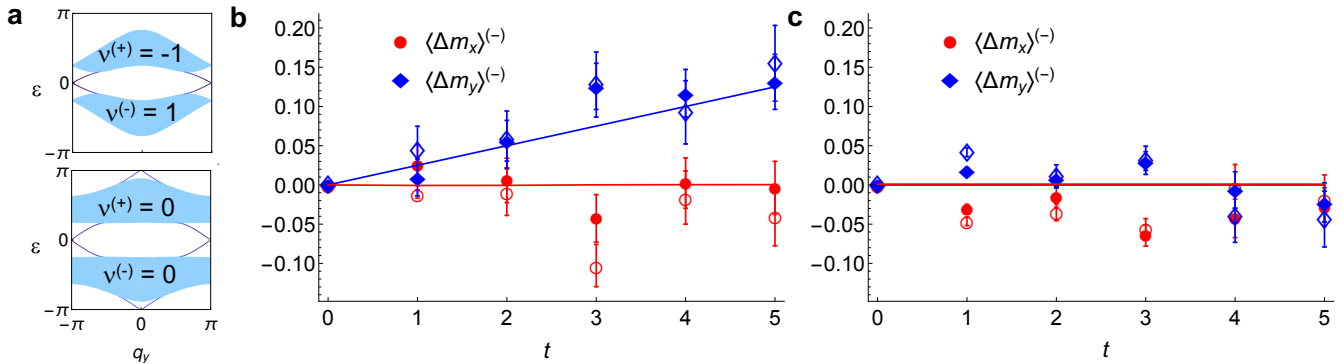


FIG. 4. **Anomalous displacement for trivial and non-trivial Chern bands.** **a**, Quasi-energy spectra computed on a cylinder open along x for $\delta = \pi/2$ (top) and $\delta = 7\pi/8$ (bottom), showing the Chern numbers ν of the various bands. In our Floquet system, edge states (shown as darker lines inside the gaps) may be present even if all bands have vanishing Chern numbers. **b**, Center-of-mass average displacement $\langle \Delta m_x \rangle^{(-)}(t)$ and $\langle \Delta m_y \rangle^{(-)}(t)$ measured for $\delta = \pi/2$ in the lower band. Empty markers show results from the simple protocol U , while solid symbols show the improved results obtained by combining protocol U with its inverse U^{-1} . Straight lines correspond to the theoretical results dictated by the semi-classical equations of motion, predicting an anomalous displacement proportional to the band Chern number. **c**, Center of mass displacements measured with $\delta = 7\pi/8$. Meaning of all symbols and lines as in panel **b**. Statistical uncertainties include estimated misalignment effects, as discussed in the Methods.

two) of the data obtained with the protocols U and U^{-1} . This procedure reduces significantly the overall displacement along x , while in the y direction we observe a very nice agreement between our data and the semi-classical predictions. The measured value of the Chern number is $\nu^{(-)} = 1.19 \pm 0.13$, consistent with the theoretical value of 1 (errors are given at one standard deviation). A similar behaviour is also observed for larger values of the force, as shown in Supplementary Fig. S8. In Fig. 4c, we replicate the same experiment for a QW with $\delta = 7\pi/8$, when the Chern numbers are zero, even though the presence of edge states witnesses non-trivial topology [43] (see also Supplementary Note 5). In agreement with the prediction of vanishing anomalous displacement, the average wavepacket motion in both directions is observed to be negligible, yielding a Chern number $\nu^{(-)} = 0.10 \pm 0.15$.

III. DISCUSSION

In this work we have experimentally demonstrated a conceptually new scheme for the realization of a 2D discrete-time quantum walk, that relies on encoding the walker and the coin systems into the transverse momentum of photons and in their polarization, respectively. The coin rotation and shift operators are implemented by suitably engineered liquid crystals plates, whose number scales linearly with the number of time-steps. They are arranged in a compact set-up, in which multiple degrees of freedom can be controlled dynamically, such as the plates optical retardation δ or their transverse position, allowing one to study several quantum walk architectures. If needed, different LC patterns could be written onto the plates, yielding different types of quan-

tum dynamics. The platform accurately simulates the dynamics dictated by the quantum walk protocols that we tested, as witnessed by the good agreement between measured distributions and numerical results. We investigated 2D walks of both localized and extended inputs, with and without an external force. The 2D protocol we presented here simulates a Floquet Chern insulator. We probed the associated topological features by preparing wave-packets which well approximate the eigenstates of the QW Floquet Hamiltonian, and detecting their average anomalous displacement arising when a constant force is applied to the system.

The set-up has been designed to minimize the decoherence effects caused by light diffraction and walk-off phase delays occurring when the walker follows different paths (see Supplementary Note 7). There is no fundamental limitation to scaling up our set-up to a much larger number of steps. The efficiency of a single step is currently mainly limited by the LC plates reflection losses ($\simeq 15\%$ at each plate), which could be greatly reduced by applying a standard anti-reflection coating. This would make the system suitable for single photons quantum experiments.

In prospect, diverse directions could be investigated with our platform, such as the realization of 2D lattices with more complex topologies (for example, hexagonal), or experiments in the multi-photon regime, for instance in the context of QW applications to Boson sampling. Direct access to both walker position and quasi-momentum could be exploited to study complex dynamics in the regime of spatial disorder. By combining topology and our dynamical control of the system parameters, we could investigate dynamical quantum phase transitions in quantum walks [44–46]. The demonstration of a

new platform for 2D quantum walks opens the door to the experimental study of this simple yet rich quantum dynamics in two spatial dimensions, with potential applications to diverse scenarios like the topological physics of 2D periodically-driven systems [29, 30].

ACKNOWLEDGMENTS

AD'E, FC, RB and LM acknowledge financial support from the European Union Horizon 2020 program, under European Research Council (ERC) grant no. 694683 (PHOSPhOR). ADa, MM, PM and ML acknowledge Spanish MINECO (Severo Ochoa SEV-2015-0522, FisicaTeAMO FIS2016-79508-P, and SWUQM FIS2017-84114-C2-1-P), the Generalitat de Catalunya (SGR874 and CERCA), the EU (ERC AdG OSYRIS 339106, H2020-FETProAct QUIC 641122), the Fundació Privada Cellex, a Cellex-ICFO-MPQ fellowship, the "Juan de la Cierva" program (IJCI-2017-33180) and the "Ramón y Cajal" program.

IV. METHODS

A. LC plates

The optical action of our LC plates with generic retardation δ and optic axis orientation α is described by the operator $L(\delta, \alpha)$, which in the basis of circular polarizations is defined by:

$$\begin{aligned} L(\delta, \alpha)|L\rangle &= \cos(\delta/2)|L\rangle + i \sin(\delta/2)e^{i2\alpha}|R\rangle; \\ L(\delta, \alpha)|R\rangle &= \cos(\delta/2)|R\rangle + i \sin(\delta/2)e^{-i2\alpha}|L\rangle. \end{aligned} \quad (10)$$

Coin and shifts operators can be realized by engineering suitably $\alpha(x, y)$ and δ . Inserting in Eq. (10) the appropriate expressions of α and δ one easily gets operators $T_{x,y}$ and W as given in Eqs. (3)-(4). For example, $T_x(\delta, \alpha_0) = L(\delta, \pi x/\Lambda + \alpha_0)$.

B. Spatial coordinates on the camera

Let us denote by \mathbf{R} the position on the camera plane, where we image the space of light transverse momentum by means of a lens with focal length f . The relation mapping transverse momentum \mathbf{k}_\perp to \mathbf{R} is:

$$\mathbf{R} = \frac{f\lambda \mathbf{k}_\perp}{2\pi} \quad (11)$$

and can be used any time it is required to convert \mathbf{k}_\perp into a distance along the focal plane.

C. Applying a constant force

A constant force along the lattice x direction is implemented by a modified single-step operator, whose expression in quasi-momentum space is:

$$\tilde{U}(\mathbf{q}', \mathbf{q}, t) = \delta(q'_x - q_x + F_x t) \delta(q'_y - q_y) U(q_x + F_x t, q_y),$$

where $\delta(\cdot)$ denotes the Dirac delta function and $U(\mathbf{q})$ is the single-step coin operator without force for a given quasi-momentum \mathbf{q} . We also have

$$U(q_x + F_x t, q_y) = T_y(\mathbf{q}) e^{it \frac{F_x}{2} \sigma_z} T_x(\mathbf{q}) e^{-it \frac{F_x}{2} \sigma_z} W.$$

The operator $e^{it \frac{F_x}{2} \sigma_z} T_x(\delta, \alpha_0) e^{-it \frac{F_x}{2} \sigma_z} = T_x(\delta, \alpha_0 - tF_x/2) = L(\delta, \pi x/\Lambda + \alpha_0 - tF_x/2)$ is obtained by shifting a g -plate by $\Delta x = tF_x \Lambda / (2\pi)$ along the x axis, which corresponds to the transformation $x \rightarrow x - \Delta x$. The same reference-system transformation realizes also the operation $q_x \rightarrow q_x + F_x t$ in quasi-momentum space.

D. Inverse protocol U^{-1}

The inverse protocol U^{-1} is obtained by properly tuning the plate retardations. Since $L(\delta_1)L(\delta_2) = L(\delta_1 + \delta_2)$ and $L(2\pi)$ is the identity operator (up to a global phase factor), the inverse operator is simply $L^{-1}(\delta) = L(2\pi - \delta)$. Recalling that $W = L(\pi/2, 0)$ [see Eq. (10)] and that $U = T_y(\delta)T_x(\delta)W$, it is straightforward to show that $U^{-1} = L(3/2\pi, 0)T_x(2\pi - \delta)T_y(2\pi - \delta)$.

E. Error analysis in wavepackets experiments

A systematic error that can affect our set-up is related to the possible misalignments of g -plates in both x and y directions. Our platform allows adjusting their x position only. As such, by repeating the experiment after re-aligning these plates, we can estimate the associated standard error. It is not possible however to repeat the same procedure for the perpendicular direction. In this case, after measuring the effective displacements of the T_y plates, that are determined by fabrication imperfections, we perform a Montecarlo simulation of our wavepacket QW propagation and estimate the standard deviation of the final center of mass position. The two errors are finally combined by adding their variances to obtain the error bars in Figs. 3,4 and in Supplementary Fig. S8.

[1] Venegas-Andraca, S. E., *Quantum walks: a comprehensive review*, *Quantum Inf. Process.* **11**, 1015 (2012).

[2] Shenvi, N., Kempe, J. and Whaley, K. B., *Quantum random-walk search algorithm*, *Phys. Rev. A* **67**, 052307

- (2003).
- [3] Childs, A. M., *Universal Computation by Quantum Walk*, *Phys. Rev. Lett.* **102**, 180501 (2009).
 - [4] Mohseni, M., Reberntrost, P., Lloyd, S. and Aspuru-Guzik, A., *Environment-assisted quantum walks in photosynthetic energy transfer*, *J. Chem. Phys.* **129**, 174106 (2008).
 - [5] Kitagawa, T., Rudner, M. S., Berg, E. and Demler, E., *Exploring Topological Phases With Quantum Walks*, *Phys. Rev. A* **82**, 1 (2010).
 - [6] Karski, M. *et al.*, *Quantum Walk in Position Space with Single Optically Trapped Atoms*, *Science* **325**, 174 (2009).
 - [7] Genske, M. *et al.*, *Electric quantum walks with individual atoms*, *Phys. Rev. Lett.* **110**, 190601 (2013).
 - [8] Preiss, P. M. *et al.*, *Strongly correlated quantum walks in optical lattices*, *Science* **347**, 1229 (2015).
 - [9] Dadras, S., Gresch, A., Groiseau, C., Wimberger, S. and Summy, G. S., *Quantum Walk in Momentum Space with a Bose-Einstein Condensate*, *Phys. Rev. Lett.* **121**, 070402 (2018).
 - [10] Flurin, E. *et al.*, *Observing Topological Invariants Using Quantum Walks in Superconducting Circuits*, *Phys. Rev. X* **7**, 031023 (2017).
 - [11] Broome, M. a. *et al.*, *Discrete Single-Photon Quantum Walks with Tunable Decoherence*, *Phys. Rev. Lett.* **104**, 153602 (2010).
 - [12] Peruzzo, A. *et al.*, *Quantum Walks of Correlated Photons*, *Science* **329**, 1500 (2010).
 - [13] Sansoni, L. *et al.*, *Two-Particle Bosonic-Fermionic Quantum Walk via Integrated Photonics*, *Phys. Rev. Lett.* **108**, 010502 (2012).
 - [14] Schreiber, A. *et al.*, *A 2D Quantum Walk Simulation of Two-Particle Dynamics*, *Science* **336**, 55 (2012).
 - [15] Cardano, F. *et al.*, *Quantum walks and wavepacket dynamics on a lattice with twisted photons*, *Sci. Adv.* **1**, e1500087 (2015).
 - [16] Defienne, H., Barbieri, M., Walmsley, I. A., Smith, B. J. and Gigan, S., *Two-photon quantum walk in a multimode fiber*, *Sci. Adv.* **2**, e1501054 (2016).
 - [17] Schreiber, A. *et al.*, *Decoherence and Disorder in Quantum Walks: From Ballistic Spread to Localization*, *Phys. Rev. Lett.* **106**, 180403 (2011).
 - [18] Jeong, Y.-C., Di Franco, C., Lim, H.-T., Kim, M. and Kim, Y.-H., *Experimental realization of a delayed-choice quantum walk*, *Nat. Commun.* **4**, 2471 (2013).
 - [19] Kitagawa, T. *et al.*, *Observation of topologically protected bound states in photonic quantum walks*, *Nat. Commun.* **3**, 882 (2012).
 - [20] Poullos, K. *et al.*, *Quantum Walks of Correlated Photon Pairs in Two-Dimensional Waveguide Arrays*, *Phys. Rev. Lett.* **112**, 143604 (2014).
 - [21] Crespi, A. *et al.*, *Anderson localization of entangled photons in an integrated quantum walk*, *Nat. Photon.* **7**, 322 (2013).
 - [22] Harris, N. C. *et al.*, *Quantum transport simulations in a programmable nanophotonic processor*, *Nat. Photon.* **11**, 447 (2017).
 - [23] Zeuner, J. M. *et al.*, *Observation of a Topological Transition in the Bulk of a Non-Hermitian System*, *Phys. Rev. Lett.* **115**, 040402 (2015).
 - [24] Cardano, F. *et al.*, *Dynamical moments reveal a topological quantum transition in a photonic quantum walk*, *Nat. Commun.* **7**, 11439 (2015).
 - [25] Cardano, F. *et al.*, *Detection of Zak phases and topological invariants in a chiral quantum walk of twisted photons*, *Nat. Commun.* **8**, 15516 (2017).
 - [26] Xiao, L. *et al.*, *Observation of topological edge states in parity-time-symmetric quantum walks*, *Nat. Phys.* **13**, 1117 (2017).
 - [27] Zhan, X. *et al.*, *Detecting Topological Invariants in Nonunitary Discrete-Time Quantum Walks*, *Phys. Rev. Lett.* **119**, 130501 (2017).
 - [28] Ozawa, T. *et al.*, *Topological Photonics*, [arXiv:1802.04173](https://arxiv.org/abs/1802.04173) (2018).
 - [29] Chen, C. *et al.*, *Observation of Topologically Protected Edge States in a Photonic Two-Dimensional Quantum Walk*, *Phys. Rev. Lett.* **121**, 100502 (2018).
 - [30] Wang, B., Chen, T. and Zhang, X., *Experimental Observation of Topologically Protected Bound States with Vanishing Chern Numbers in a Two-Dimensional Quantum Walk*, *Phys. Rev. Lett.* **121**, 100501 (2018).
 - [31] Tang, H. *et al.*, *Experimental two-dimensional quantum walk on a photonic chip*, *Sci. Adv.* **4**, eaat3174 (2018).
 - [32] Tang, H. *et al.*, *Experimental quantum fast hitting on hexagonal graphs*, *Nat. Photon.* **32**, 534 (2018).
 - [33] Marrucci, L., Manzo, C. and Paparo, D., *Optical Spin-to-Orbital Angular Momentum Conversion in Inhomogeneous Anisotropic Media*, *Phys. Rev. Lett.* **96**, 163905 (2006).
 - [34] Di Franco, C., Mc Gettrick, M. and Busch, T., *Mimicking the Probability Distribution of a Two-Dimensional Grover Walk with a Single-Qubit Coin*, *Phys. Rev. Lett.* **106**, 080502 (2011).
 - [35] Di Franco, C., Mc Gettrick, M., Machida, T. and Busch, T., *Alternate two-dimensional quantum walk with a single-qubit coin*, *Phys. Rev. A* **84**, 042337 (2011).
 - [36] Aharonov, Y., Davidovich, L. and Zagury, N., *Quantum random walks*, *Phys. Rev. A* **48**, 1687 (1993).
 - [37] Edge, J. M. and Asboth, J. K., *Localization, delocalization, and topological transitions in disordered two-dimensional quantum walks*, *Phys. Rev. B* **91**, 104202 (2015).
 - [38] Piccirillo, B., D'Ambrosio, V., Slussarenko, S., Marrucci, L. and Santamato, E., *Photon spin-to-orbital angular momentum conversion via an electrically tunable Si -plate*, *Appl. Phys. Lett.* **97**, 4085 (2010).
 - [39] Qi, X.-L., Hughes, T. L. and Zhang, S.-C., *Topological field theory of time-reversal invariant insulators*, *Phys. Rev. B* **78**, 195424 (2008).
 - [40] Xiao, D., Chang, M.-C. and Niu, Q., *Berry phase effects on electronic properties*, *Rev. Mod. Phys.* **82**, 1959 (2010).
 - [41] Price, H. M., Zilberberg, O., Ozawa, T., Carusotto, I. and Goldman, N., *Measurement of Chern numbers through center-of-mass responses*, *Phys. Rev. B* **93**, 245113 (2016).
 - [42] Dauphin, A. and Goldman, N., *Extracting the Chern Number from the Dynamics of a Fermi Gas: Implementing a Quantum Hall Bar for Cold Atoms*, *Phys. Rev. Lett.* **111**, 135302 (2013).
 - [43] Rudner, M. S., Lindner, N. H., Berg, E. and Levin, M., *Anomalous Edge States and the Bulk-Edge Correspondence for Periodically Driven Two-Dimensional Systems*, *Phys. Rev. X* **3**, 031005 (2013).
 - [44] Wang, K. *et al.*, *Simulating dynamic quantum phase transitions in photonic quantum walks*, [arXiv:1806.10871](https://arxiv.org/abs/1806.10871) (2018).

- [45] Xu, X.-Y. *et al.*, *Measuring a Dynamical Topological Order Parameter in Quantum Walks*, [arXiv:1808.03930](#) (2018).
- [46] Heyl, M., *Dynamical quantum phase transitions: a review*, [Rep. Prog. Phys.](#) **81**, 054001 (2018).
- [47] Budich, J. C., Hu, Y. and Zoller, P., *Helical Floquet Channels in 1D Lattices*, [Phys. Rev. Lett.](#) **118**, 105302 (2017).
- [48] Nathan, F. and Rudner, M. S., *Topological singularities and the general classification of Floquet–Bloch systems*, [New J. Phys.](#) **17**, 125014 (2015).

Supplementary Material

Supplementary Note 1. PHOTONIC SPATIAL MODES $|\mathbf{m}\rangle$

A. Gaussian modes encoding single walker positions

The state $|\mathbf{m}, \phi\rangle$ of a walker is encoded in our set-up in a light beam described by Eq. (1),

$$|\mathbf{m}, \phi\rangle = A(x, y, z)e^{i[\Delta k_{\perp}(m_x x + m_y y) + k_z z]} \otimes |\phi\rangle, \quad (\text{S1})$$

where $\mathbf{m} = (m_x, m_y)$ are the integer coordinates giving the discrete position of the walker, and the light's polarization $|\phi\rangle$ encodes the state of the coin of the walker. The spatial profile of the beam is determined by the Gaussian envelope function

$$A(x, y, z) = \frac{w_0}{w(z)} e^{-\frac{x^2+y^2}{w(z)^2}} e^{ik\frac{x^2+y^2}{2R(z)}} e^{-i\xi(z)}, \quad (\text{S2})$$

where $k = 2\pi/\lambda$ is the wavenumber, and the beam radius $w(z)$, the beam curvature $R(z)$ and the Gouy phase $\xi(z)$ are defined as follows:

$$w(z) = w_0 \sqrt{1 + (z/z_0)^2}, \quad (\text{S3})$$

$$R(z) = z[1 + (z_0/z)^2], \quad (\text{S4})$$

$$\xi(z) = \arctan(z/z_0). \quad (\text{S5})$$

Here $w_0 = w(z=0)$ is the beam radius at the waist position $z=0$, and the parameter $z_0 = \pi w_0^2/\lambda$ is known as Rayleigh range. In our experiment, we set $w_0 = 5$ mm, which yields $z_0 \approx 120$ m, so that across the whole QW setup (about 30 cm long) the beam radius is approximately constant ($w(z) \approx w_0$), and both the Gouy phase $\xi(z)$ and the inverse beam curvature $1/R(z)$ are entirely negligible.

If we place a converging lens at the end of the quantum walk, in the focal plane the field distribution is proportional to the distribution of the transverse wavevector, that is:

$$A(X, Y) \propto \int_{\Omega} A(x, y, d) e^{i[\Delta k_{\perp}(m_x x + m_y y) + k_z d]} e^{i(Xx + Yy)k/f} dx dy, \quad (\text{S6})$$

where Ω is the transverse plane, d the distance of the lens from the beam waist, f the focal length of the lens, and $\mathbf{R} = (X, Y)$ the spatial coordinates in the focal plane of the lens. It is well known that, independently of the distance d , in the focal plane the field intensity is proportional to the Fourier transform of the field impinging on the lens, that is

$$|A(X, Y)|^2 \propto |g(k_x, k_y)|^2 \quad (\text{S7})$$

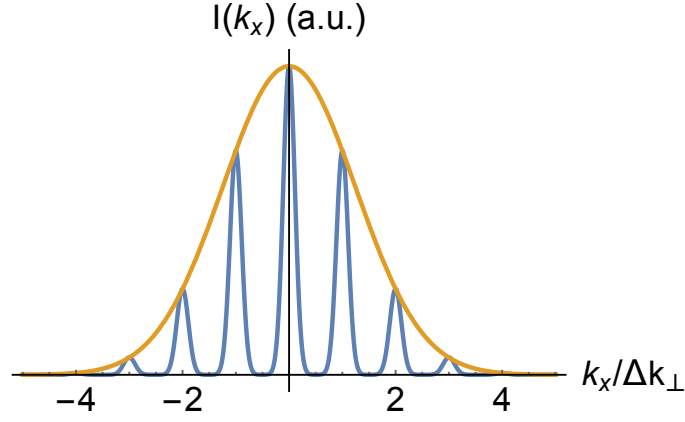
where $g(k_x, k_y)$ is the Fourier transform of $A(x, y)$, provided that one sets $X = k_x f/k$ and $Y = k_y f/k$. In the case of a Gaussian beam, we have

$$|A(X, Y)|^2 \propto e^{\left(-2\frac{(m_x \Delta k_{\perp} - kX/f)^2 + (m_y \Delta k_{\perp} - kY/f)^2}{\tilde{w}_k^2}\right)}, \quad (\text{S8})$$

with $\tilde{w}_k = 2/w_0$. Thus \tilde{w}_k is a measure of the radius of the spots that appear in the focal plane, provided that one uses Eq. (11) to convert photons transverse momentum into a position on the camera.

B. Extended wavepacket walker states and their optical implementation

As discussed above, attention must be paid to the beam radius of modes $|\mathbf{m}\rangle$. Indeed, once the lattice spacing Δk_{\perp} is fixed, w_0 must be selected so that the overlap between adjacent modes is negligible. In our set-up, $\Lambda = 5$ mm and our choice of setting the beam waist to $w_0 = 5$ mm leads to an overlap between adjacent modes of around 0.8%. In general, initial states other than localized ones can be prepared, such as for instance Gaussian wavepackets



Supplementary Figure S1. **Gaussian wavepackets.** Comparison between the intensity distribution $I(k_x)$ (we set $k_y=0$) of the wavepacket states $|G\rangle$ (blue curve), with $\sigma_G = 2.5$, and of a single Gaussian mode $|\Psi_g\rangle$ (orange curve), whose beam radius in Fourier space is $\tilde{\sigma}_G = \sigma_G \Delta k_\perp$. In this plot, individual modes $|\mathbf{m}\rangle$ contained in $|G\rangle$ are characterized by their actual beam radius $w_k = 0.23 \Delta k_\perp$.

$|G\rangle = \mathcal{N} \sum_{\mathbf{m}} |\mathbf{m}\rangle e^{-(m_x^2 + m_y^2)/\sigma_G^2}$, where \mathcal{N} is a normalization factor and σ_G is the width of the overall Gaussian envelope (in dimensionless units). In Supplementary Fig. S1, we plot a 1D cut of the corresponding beam-intensity wavevector profile versus k_x , at $k_y = 0$ (blue curve), showing several peaks modulated by a Gaussian envelope, each peak corresponding to a mode $|\mathbf{m}\rangle$ included in the wavepacket. The QW dynamics of such an input state is equivalent to that of a single Gaussian beam $|\Psi_g\rangle$, whose beam radius is $w_g = 2/(\sigma_G \Delta k_\perp)$. The preparation of such a state is much simpler, since it requires a modulation of the beam radius only, which is simply achieved with a confocal pair of lenses. In Supplementary Fig. S1 we provide a comparison between the intensity distribution associated with $|G\rangle$ (blue curve) and $|\Psi_g\rangle$ (orange curve).

In our experiments, we are particularly interested at wavepackets $\mathcal{N} \sum_{\mathbf{m}} |\mathbf{m}\rangle e^{i\mathbf{q}_0 \cdot \mathbf{m}} e^{-(m_x^2 + m_y^2)/\sigma_G^2}$, that include the phase factor $e^{i\mathbf{q}_0 \cdot \mathbf{m}}$. Indeed, in quasi-momentum space these feature a Gaussian distribution with $\tilde{\sigma}_G = 2/\sigma_G$, peaked around a specific quasi-momentum \mathbf{q}_0 . Their expression reads

$$|\Psi_g(\mathbf{q}_0)\rangle = \mathcal{N}' \int_{\text{BZ}} \frac{d^2 \mathbf{q}}{4\pi^2} e^{-\frac{(\mathbf{q}-\mathbf{q}_0)^2}{\sigma_G^2}} |\mathbf{q}\rangle, \quad (\text{S9})$$

where \mathcal{N}' is a normalization factor, and $\text{BZ} = [-\pi, \pi]^2$ is the Brillouin zone. We want these beams to be sharply peaked, that is $\tilde{\sigma}_G \ll 1$, so that they approximate as much as possible the individual state $|\mathbf{q}_0\rangle$. Being the simulated quasi-momentum encoded in the physical transverse position \mathbf{r}_\perp , these wavepackets are realized by standard Gaussian beams, whose central position is set to $\mathbf{r}_\perp = -\Lambda \mathbf{q}_0 / (2\pi)$, and which are characterized by a beam radius that is much smaller than the spatial period Λ .

In the focal plane of the lens, these beams display a continuous distribution, as shown for instance in Fig. 3b. Being sharply peaked in the space of the walker quasi-momentum, we expect them to cover multiple lattice sites in the space of walker position. If one is interested in obtaining the associated walker probability distribution, our standard procedure described in Supplementary Note 3 can be applied. However, in our experiments, we are interested in detecting the wavepacket center of mass, which can be determined by analyzing directly the overall intensity pattern recorded by the camera.

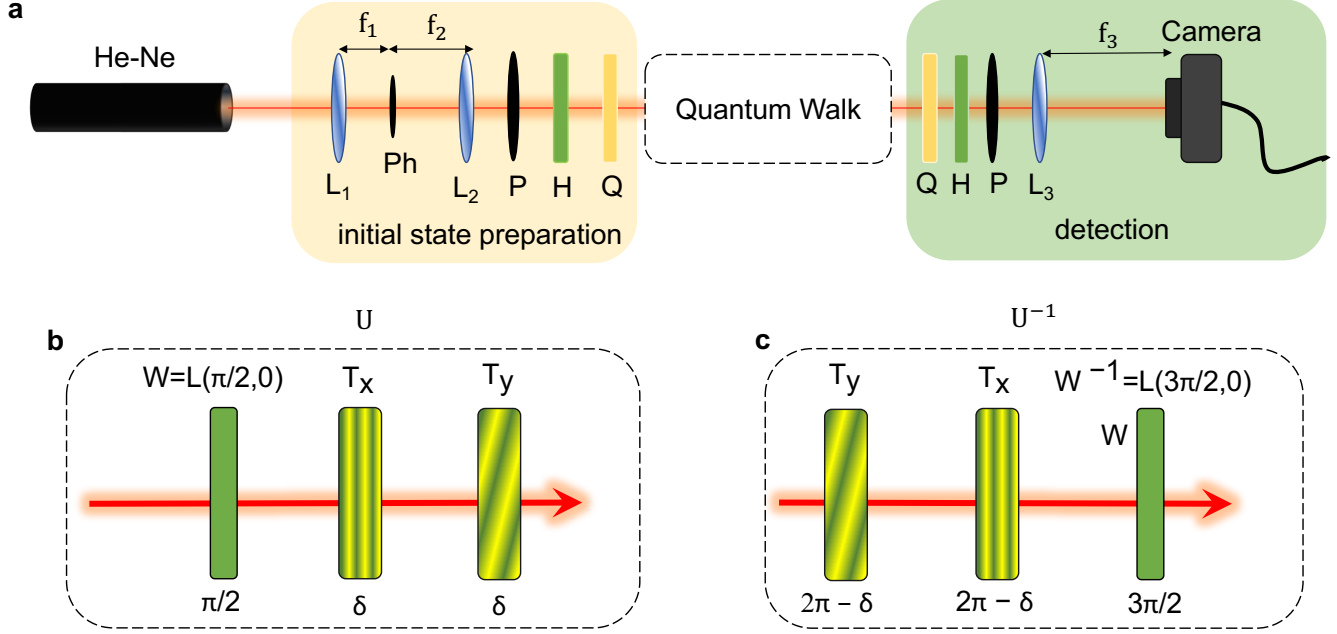
As shown in the main text, we use these beams to prepare photonic states:

$$|\Psi_g(\mathbf{q}_0, \pm)\rangle = |\Psi_g(\mathbf{q}_0)\rangle \otimes |\phi_\pm(\mathbf{q}_0)\rangle \quad (\text{S10})$$

where the coin part corresponds to the eigenstates $|\phi_\pm(\mathbf{q}_0)\rangle$ of the effective Hamiltonian. These states are extremely useful to probe the QW dispersion and the associated topological features (see Figs. 3,4).

Supplementary Note 2. DETAILS OF THE EXPERIMENTAL PLATFORM

A complete scheme of the set-up implementing our QW dynamics is reported in Supplementary Fig. S2a. A laser beam is produced by a Helium:Neon source with wavelength $\lambda = 632.8$ nm, and propagates along the \hat{z} direction.

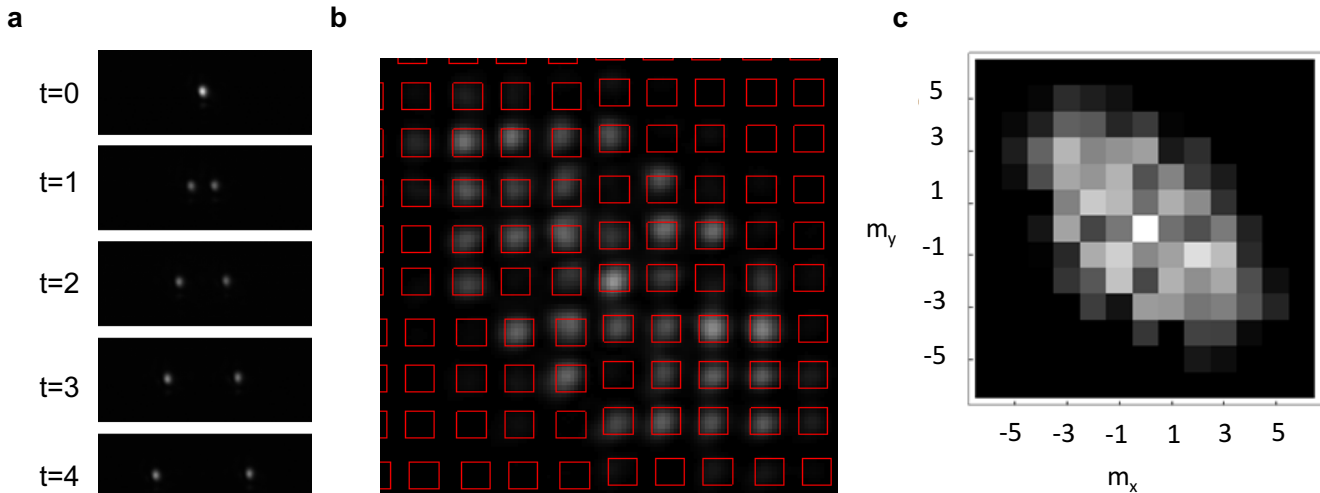


Supplementary Figure S2. **Details of the experimental set-up and protocols.** **a.** Sketch of the experimental set-up. The waist of a laser beam emitted from a He-Ne laser is modified with a pair of convex lenses L_1 and L_2 , with focal lengths f_1 and f_2 . A pinhole (Ph), placed in the common focus of the two lenses, is used as spatial filter to erase higher-order spatial frequencies. The polarization of the input state is selected by means of a polarizer (P), a half-wave plate (H) and a quarter-wave plate (Q). These wave plates are mounted on motorized rotation stages allowing for automatic selection of the coin states. After the QW an additional set of waveplates can be used to analyze the probability distributions of specific polarization components. The probability distribution is visualized by focusing the laser beam on a camera with a lens L_3 of focal length $f_3 = 50$ cm. **b.** A single step of our QW with protocol U is obtained by cascading three optical plates: a spin rotation W , followed by a coin-conditioned translation along x and another along y , with optical retardations δ as indicated below every device. **c.** Set-up yielding a single step of the inverse protocol U^{-1} .

We use a system of two lenses and a pinhole (L_1 , Ph, L_2) to set the beam waist to $w_0 = (5.0 \pm 0.2)$ mm or to $w_0 = (0.62 \pm 0.02)$ mm, depending on our necessity to start the walk with either “localized states” or “extended wave-packets”, respectively (See [Supplementary Note 1](#) for further details on the spatial features of the light beam). In the last stage of the preparation, a polarizer and two waveplates (P,H,Q) are used to prepare a given polarization.

The beam undergoes the proposed QW dynamics by passing through a sequence of wave-plates and g -plates. In panels **b** and **c** we display the combination of plates realizing the protocols U and U^{-1} , respectively. All operators are physically implemented by thin optical plates, which allows us to mount them in a very compact mechanical holder realized by a 3D printing technique. The distance between consecutive steps is currently $\simeq 2$ cm, yet it could be significantly reduced by optimizing the thickness of the glass and of the plastic mounts. Within each plate, the active layer containing liquid crystals (LCs) is $6 \mu\text{m}$ thick. The spatial period of g -plates pattern is $\Lambda = 5$ mm, yielding a transverse momentum displacement of $\Delta k_{\perp} = 2\pi/\Lambda = 1.26$ (mm) $^{-1}$, that provides the spacing between neighbouring sites in our squared lattice. In order to have each mode $|\mathbf{m}\rangle$ entirely localized on the associated site (m_x, m_y) , without “cross-talk”, the single-mode beam radius w_0 must be properly selected. In Fourier space, where the lattice of walker positions is defined, these beams are characterized by a radius $w_k = \sqrt{2}/w_0$. If one chooses $w_0 \simeq \Lambda$, one gets that the ratio between the beam radius (in Fourier space) and the lattice spacing $w_k/\Delta k_{\perp} \simeq 1/\pi = 0.32$ is sufficiently small and the overlap between adjacent modes is negligible (see Fig. [1b](#)).

At the exit of the walk, two wave-plates and one polarizer (Q,H,P) are used to analyze individual polarization components. Finally a lens (L_3) focuses the field on a camera that records the distribution of light intensity, operating an all-optical Fourier transform. In the focal plane, light is spread over several spots, according to the walker distribution over the lattice. A single image contains the overall probability distribution, and the latter can be monitored in real time. Since the Rayleigh range of the input beam is much longer than the total distance of the walk (see [Supplementary Note 1](#)), the latter takes place in the near field and the beam remains collimated.



Supplementary Figure S3. **Extracting probability distributions from the recorded intensity patterns.** **a**, Sample intensity patterns obtained with the simple protocol $U = S_x(\pi) \cdot H_{wp}$. An input linearly polarized state is split into two spots with opposite circular polarizations. At each step these spots are shifted by a quantity corresponding to the equivalent of a lattice spacing. This process can be used to identify the coordinates of the lattice sites on the camera, getting rid of some of the experimental imperfections explained in the text. Panels **b** and **c** show the procedure used to extract the probability distributions from the intensity patterns. The red squares in **b** represent the regions over which we obtain the total intensities (= powers) associated to specific lattice sites (since the single spots occupy a small number of pixels there is no substantial difference in using square or circular integration regions). Normalizing to 1 the sum of all these intensities we obtain the probability distribution shown in panel **c**.

Supplementary Note 3. EXTRACTION OF THE PROBABILITY DISTRIBUTIONS FROM THE INTENSITY PATTERNS

When injecting modes with beam radius $w_0 \simeq 5$ mm, at the end of the walk we record the light intensity in the focal plane of the camera, that is distributed over many spots corresponding to the walker lattice sites. The probability distribution of the associated quantum walk can be extracted by measuring the amount of light in each region. In principle, the lattice site positions on the camera could be determined by (i) individuating the axes origin $(0,0)$ (setting all g -plates at $\delta = 0$, so that a single spot appears on the camera), and (ii) determining the expected positions of the other sites in terms of the spacing Δk_{\perp} . However, imperfections of all plates can cause small deviations between actual spot positions and the expected ones. For instance, one contribution can be ascribed to undesired modulations in the g -plates patterns, that can be modelled by the local optic axis orientation $\alpha(x, y) = \alpha_0 + (\Delta k_{\perp}/2)x + \epsilon(x, y)$, where $\epsilon(x, y)$ is a small random error. Another source of errors can be a small tilt in the polarization gratings, so that the coordinate x in $\alpha(x)$ should be replaced by $x' = \cos(\theta)x + \sin(\theta)y$ (with θ small, and different for each grating).

To improve the calibration procedure, we follow therefore a different approach, which is illustrated in Supplementary Fig. S3. Let us first consider the 1D set-up defined by the single step operator $U_x = T_x(\delta = \pi) \cdot H_{wp}$, where H_{wp} is a half-waveplate (that can be described by the operator σ_x). This protocol simulates a recently proposed system where a spin-momentum locking effect has been predicted [47]. The particle dynamics, shown in Supplementary Fig. S3a, is indeed very simple: at each step the positions of L/R polarized components are shifted respectively by ± 1 . If we start with a linearly polarized input beam, in the following steps we will see two spots (with opposite circular polarizations), which will be located, at the time t , at the effective positions $m_x = t$ and $m_x = -t$, respectively. In this way we reconstruct the coordinates of each site by performing Gaussian fits for the two spots. By repeating the same analysis with the protocol $U_y = T_y W$ we measure the y coordinate of each site. In the actual set-up, we can realize both protocols U_x and U_y by turning off ($\delta = 0$) plates T_x or T_y . After the site coordinates have been determined, we draw squared regions around each point (see Supplementary Fig. S3b). Light detected within one of these regions is automatically associated to the corresponding lattice sites. By integrating the light intensity measured within each square, and by dividing each of these values by their total sum, we obtain a properly normalized probability distribution for the walker position (see Supplementary Fig. S3c).

Supplementary Note 4. OPERATORS IN QUASI-MOMENTUM SPACE AND DISPLACEMENT OF A WAVEPACKET IN THE PRESENCE OF A CONSTANT FORCE

We analyze the building blocks of the quantum walk in the reciprocal quasi-momentum space. For the W operator defined in Eq. (4) of the main text, the expression remains the same, as it does not depend on the position:

$$W = e^{i\frac{\pi}{4}\sigma_x} = \frac{1}{\sqrt{2}} \begin{pmatrix} 1 & i \\ i & 1 \end{pmatrix}, \quad (\text{S11})$$

where the basis of the polarization space has been chosen to be $\{|L\rangle, |R\rangle\}$.

The operators T_x and T_y are given by the two g -plates operators described in Eq. (10). Inserting the explicit expression of the angle $\alpha(x) = x\pi/\Lambda + \alpha_0$, defined in Eq. (2) of the main text, one obtains the explicit expression of T_x in momentum space:

$$T_x(q_x) = e^{i\frac{\delta}{2}(\cos(q_x)\sigma_x - \sin(q_x)\sigma_y)} = \begin{pmatrix} \cos(\delta/2) & ie^{iq_x}\sin(\delta/2) \\ ie^{-iq_x}\sin(\delta/2) & \cos(\delta/2) \end{pmatrix}, \quad (\text{S12})$$

and similarly for T_y :

$$T_y(q_y) = e^{i\frac{\delta}{2}(\cos(q_y)\sigma_x - \sin(q_y)\sigma_y)} = \begin{pmatrix} \cos(\delta/2) & ie^{iq_y}\sin(\delta/2) \\ ie^{-iq_y}\sin(\delta/2) & \cos(\delta/2) \end{pmatrix}, \quad (\text{S13})$$

where we used the mapping $q_x = \frac{-2\pi x}{\Lambda}$, $q_y = \frac{-2\pi y}{\Lambda}$ and we set $\alpha_0 = 0$. This allows one to use the standard convention for the normalized plane waves:

$$\langle \mathbf{m} | \mathbf{q} \rangle = \frac{e^{i\mathbf{q}\cdot\mathbf{m}}}{2\pi}, \quad (\text{S14})$$

where \mathbf{q} is the quasi-momentum of the walker and \mathbf{m} is its position on the 2D lattice, according to the convention chosen in the paper. The latter gives rise to Eq. (3) of the main text. The operator implementing the potential of the constant dimensionless force, $F_x\hat{m}_x$, can be regarded as a translation of the walker's quasi-momentum component q_x of a quantity F_x at each step. This operation is nondiagonal in momentum space, so the step operator in momentum space is described by $\langle \mathbf{q}' | \tilde{U}(t) | \mathbf{q} \rangle = \tilde{U}(\mathbf{q}', \mathbf{q}, t)$, where $\tilde{U}(\mathbf{q}', \mathbf{q}, t)$ is a 2×2 matrix operating in coin space only. In turn, the latter is given by $\tilde{U}(\mathbf{q}', \mathbf{q}, t) = \delta(q'_x - q_x + F_x t) \delta(q'_y - q_y) U(q_x + F_x t, q_y)$, where $\delta(\cdot)$ denotes a Dirac delta function and $U = e^{-iH_{\text{eff}}}$ is the step operator in coin space for a given quasi-momentum $\mathbf{q} = (q_x, q_y)$ for a vanishing force. We also have

$$U(q_x + F_x t, q_y) = T_y(q_y) e^{it\frac{F_x}{2}\sigma_z} T_x(q_x) e^{-it\frac{F_x}{2}\sigma_z} W. \quad (\text{S15})$$

As discussed in the Methods, the force has been implemented experimentally by progressively displacing the g -plates without using any additional optical device: the g -plate which acts at time step t is shifted laterally along the x direction by an amount of $\Delta_x = \frac{t\Lambda F_x}{2\pi}$, which is equivalent to shifting the beam position by $-\Delta_x$ and hence

$$q_x(t) = \frac{-(x + \Delta_x)2\pi}{\Lambda} = q_{0x} + F_x t. \quad (\text{S16})$$

In the adiabatic limit within the single band approximation, the semi-classical equations of motion of a wave-packet initially peaked around an energy eigenstate $e^{i\mathbf{q}_0\cdot\mathbf{m}_0} |\phi_{\pm}(\mathbf{q}_0)\rangle$ read [40–42]

$$\begin{aligned} \dot{m}_i &= \partial_{q_i} \varepsilon_{\pm}(\mathbf{q}) - \dot{q}_j \Omega_{ij}^{(\pm)}(\mathbf{q}), \\ \dot{q}_i &= F_i. \end{aligned} \quad (\text{S17})$$

Here $\{i, j\} \in \{x, y\}$, \pm denote the upper/lower band, $\varepsilon_{\pm}(\mathbf{q}) = \pm\varepsilon(\mathbf{q})$ is the quasi-energy dispersion and $\Omega_{ij}^{(\pm)}(\mathbf{q}) = -\Omega_{ij}^{(\pm)}(\mathbf{q})$ is the Berry curvature

$$\Omega_{xy}^{(\pm)}(\mathbf{q}) = i [\partial_{q_x} \langle \phi_{\pm}(\mathbf{q}) | \partial_{q_y} \phi_{\pm}(\mathbf{q}) \rangle - \partial_{q_y} \langle \phi_{\pm}(\mathbf{q}) | \partial_{q_x} \phi_{\pm}(\mathbf{q}) \rangle], \quad (\text{S18})$$

where the $|\phi_{\pm}\rangle$ are the eigenvectors of the Bloch effective Hamiltonian H_{eff}

$$H_{\text{eff}}(\mathbf{q})|\phi_{\pm}(\mathbf{q})\rangle = \varepsilon_{\pm}(\mathbf{q})|\phi_{\pm}(\mathbf{q})\rangle. \quad (\text{S19})$$

In our two-band system, the Berry curvature can also be written as [39]

$$\Omega_{xy}^{(\pm)}(\mathbf{q}) = \pm \frac{1}{2} \mathbf{n}(\mathbf{q}) \cdot \left[\frac{\partial \mathbf{n}}{\partial q_x} \times \frac{\partial \mathbf{n}}{\partial q_y} \right], \quad (\text{S20})$$

$\mathbf{n}(\mathbf{q})$ being the unitary vector giving the Floquet Hamiltonian $H_{\text{eff}}(\mathbf{q}) = \varepsilon(\mathbf{q})\mathbf{n}(\mathbf{q}) \cdot \sigma$. Therefore, for a force in the x -direction, the semi-classical equations of motion for a wavepacket center-of-mass read

$$\dot{m}_x^{(\pm)} = \partial_{q_x} \varepsilon_{\pm}(\mathbf{q}) \quad (\text{S21})$$

$$\dot{m}_y^{(\pm)} = \partial_{q_y} \varepsilon_{\pm}(\mathbf{q}) - F_x \Omega_{yx}^{(\pm)}(\mathbf{q}) = \partial_{q_y} \varepsilon_{\pm}(\mathbf{q}) + F_x \Omega_{xy}^{(\pm)}(\mathbf{q}). \quad (\text{S22})$$

We now sum the displacement of the wavepackets located on a grid $q_{x,y} = -\pi + 2\pi i/N$, where $i = 1 \dots N$. In the limit of $N \rightarrow \infty$, the mean displacement of the sum of the wavepackets corresponds to the average displacement of a filled band, i.e.,

$$\langle \Delta m_x(t) \rangle^{(\pm)} = 0 \quad (\text{S23})$$

$$\langle \Delta m_y(t) \rangle^{(\pm)} = \frac{F_x \nu^{(\pm)}}{2\pi} t, \quad (\text{S24})$$

where the Chern number of the \pm -th band is defined as:

$$\nu^{(\pm)} = \frac{1}{2\pi} \int_{\text{BZ}} d^2 \mathbf{q} \Omega_{xy}^{(\pm)}(\mathbf{q}), \quad (\text{S25})$$

One finds that the Chern number of the lower band for $\delta = \pi/2$ is $\nu^{(-)} = 1$, so that the displacement will be positive and proportional to time in the transverse direction for a positive force. By numerical tests, we have confirmed that a finite grid with 11×11 points in the BZ is sufficient in our system to obtain a good approximation of the continuous integral over the whole BZ.

Supplementary Note 5. TOPOLOGICAL CHARACTERIZATION

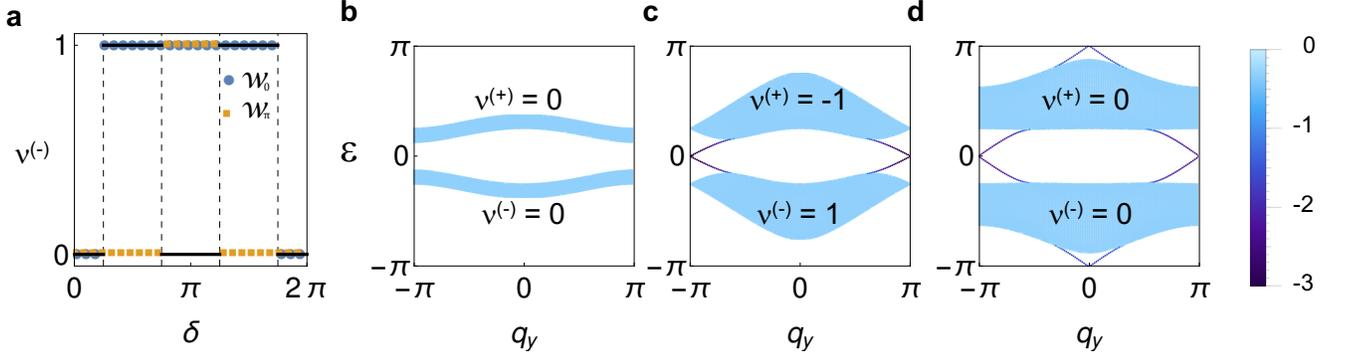
In static models, the bulk-edge correspondence guarantees that no edge modes may be present when all bands have trivial topological invariants. However, our QW protocol is described by an effective Floquet Hamiltonian. Depending on the values of δ , our effective Hamiltonian may or may not be deformed continuously into its static counterpart [25, 43, 48]. In particular, this can lead to regimes where the topological invariant of the static system, the Chern number, does not describe completely the topology of the system and does not predict the presence of protected topological edge states.

In the present work, for example, we measured the anomalous displacement of the system for two values of the parameter δ , namely $\delta = \pi/2$ and $\delta = 7\pi/8$, associated respectively with Chern numbers $\nu^{(\mp)} = \pm 1$ and $\nu^{(\mp)} = 0$. As we will see in a few lines, the latter case displays protected edge modes, even though all its bands have trivial topological invariants.

The bulk-edge correspondence of such systems was studied in detail by Rudner *et al.* in Ref. [43]. In the specific case of our model, characterized by two bands which are symmetric around zero quasi-energy, edge states may appear independently within the gap centered at quasi-energy 0, or within the gap at quasi-energy $\pm\pi$. For definiteness, figure S4a shows the Chern number of the lowest band $\nu^{(-)}$, together with the topological invariants \mathcal{W}_0 and \mathcal{W}_{π} , which count, respectively, the number of pairs of edge modes in the 0-energy and π -energy gaps. Ref. [43] provides their analytical expression, which is rather involved, but nonetheless straightforward to compute.

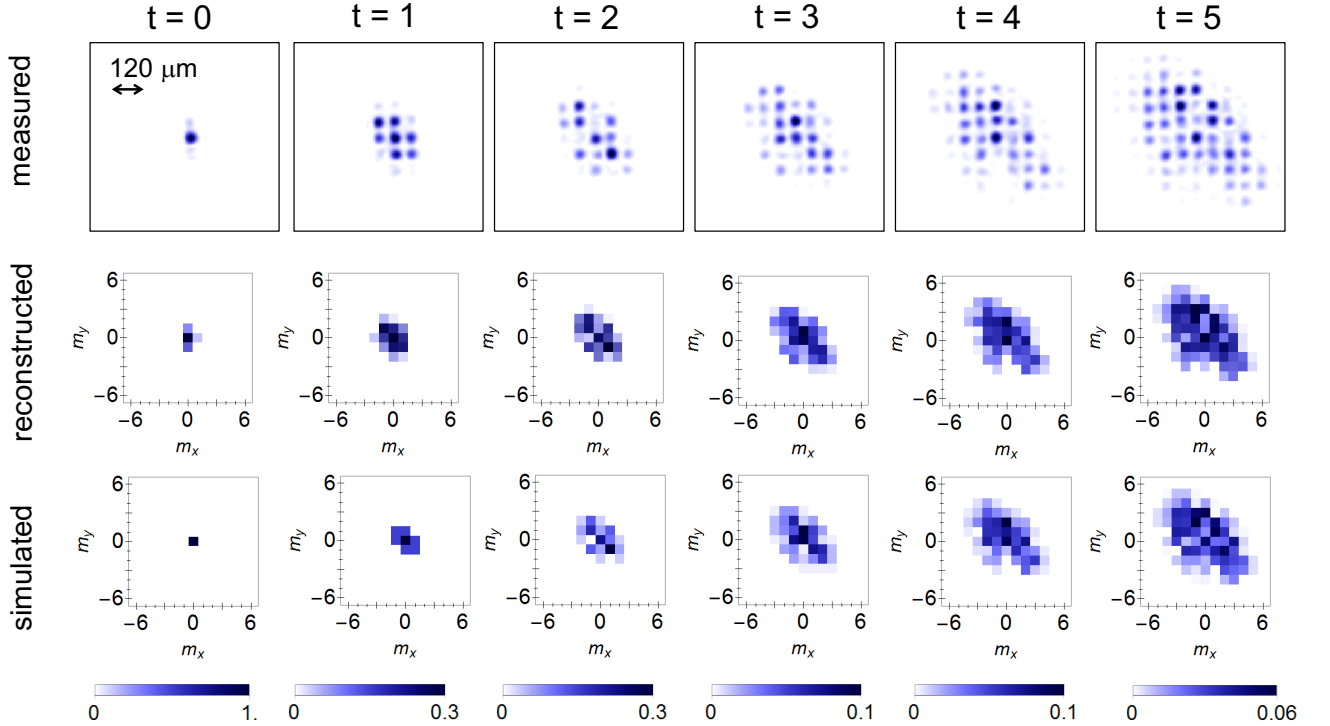
To see the emergence of edge states, Figs. S4b,c,d show the spectrum of our model on a cylinder which is open (closed) along the direction x (y), for three values of the optical retardation $\delta = \pi/8$, $\pi/2$, and $7\pi/8$. In the vicinity of $\delta = 0$ both bands have trivial Chern numbers, and no edge states are visible (see Fig. S4b). As δ is increased further, a first gap closing happens at quasi-energy 0 when $\delta = \pi/4$. As the gap re-opens, a pair of protected edge modes appear around zero-energy, and the Chern numbers switch from 0 to ± 1 (see Fig. S4c). The next gap closing happens at quasi-energy $\pm\pi$ when $\delta = 3\pi/4$. Upon re-opening of this gap, another pair of protected edge modes appears inside it, and the Chern numbers switch back from ± 1 to 0 (see Fig. S4d).

The work by Rudner *et al.* [43] in particular showed that the Chern number is related to the number of 0 and π edge modes by $\nu^{(-)} = \mathcal{W}_0 - \mathcal{W}_{\pi}$. We computed numerically these invariants for our model, and we correspondently recovered the bulk-edge correspondence, as can be seen in Fig. S4a.

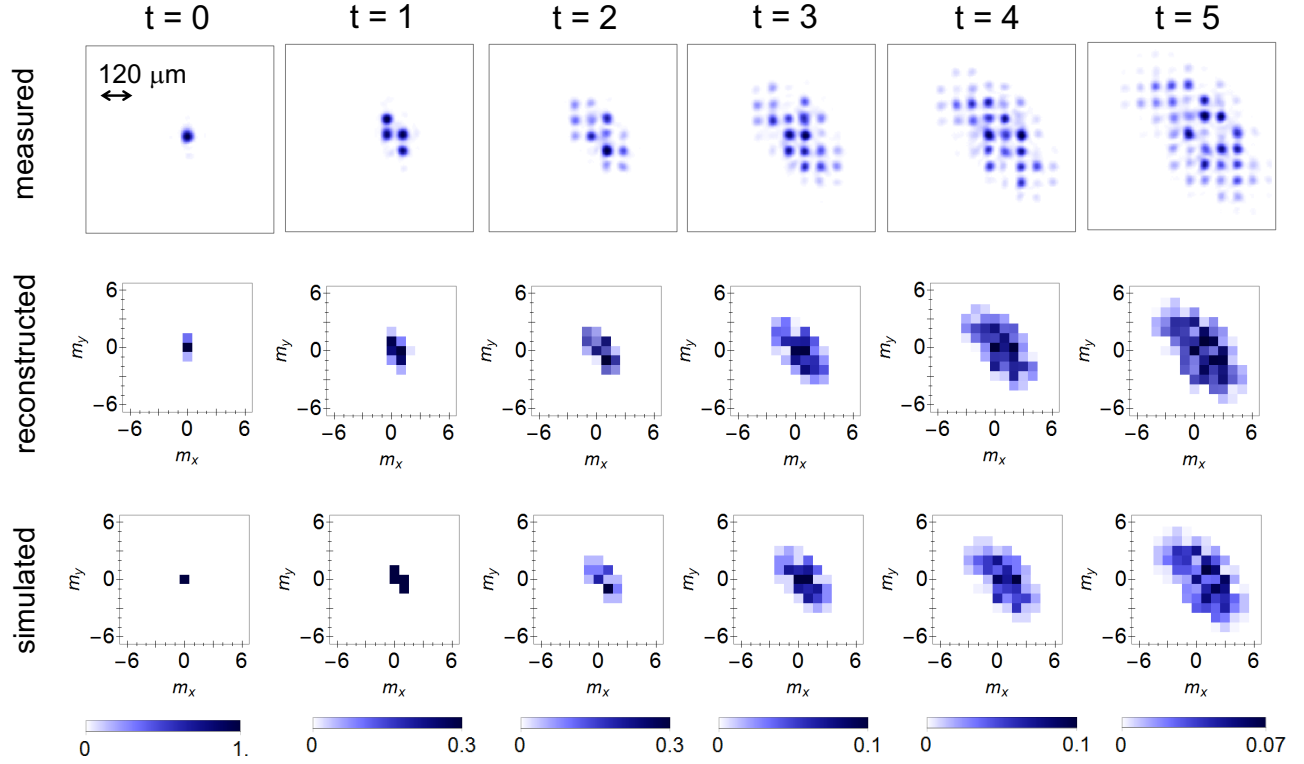


Supplementary Note 6. SUPPLEMENTARY DATA

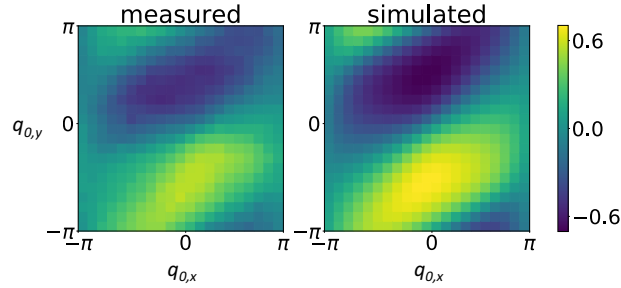
In Supplementary Figs. S5-S8, we show supplementary data supporting our results described in the main text.



Supplementary Figure S5. **2D QW for input polarization** $|A\rangle = (|L\rangle - i|R\rangle)/\sqrt{2}$. Spatial probability distributions for a quantum walk with initial condition $|0, 0, A\rangle$ and optical retardation $\delta = \pi/2$. From left to right, we display results after 0 to 5 evolution steps. Datapoints are averages of four independent measures.



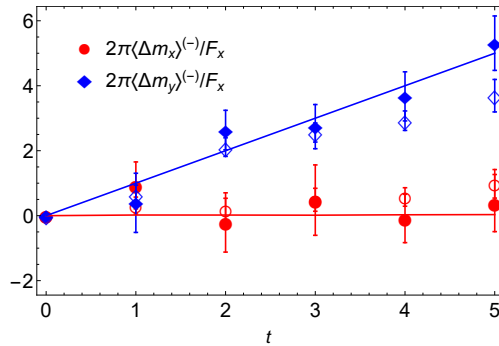
Supplementary Figure S6. **2D QW for input polarization $|L\rangle$** . Spatial probability distributions for a quantum walk with initial condition $|0, 0, L\rangle$ and optical retardation $\delta = \pi/2$. From left to right, we display results after 0 to 5 evolution steps. Datapoints are averages of four independent measures.



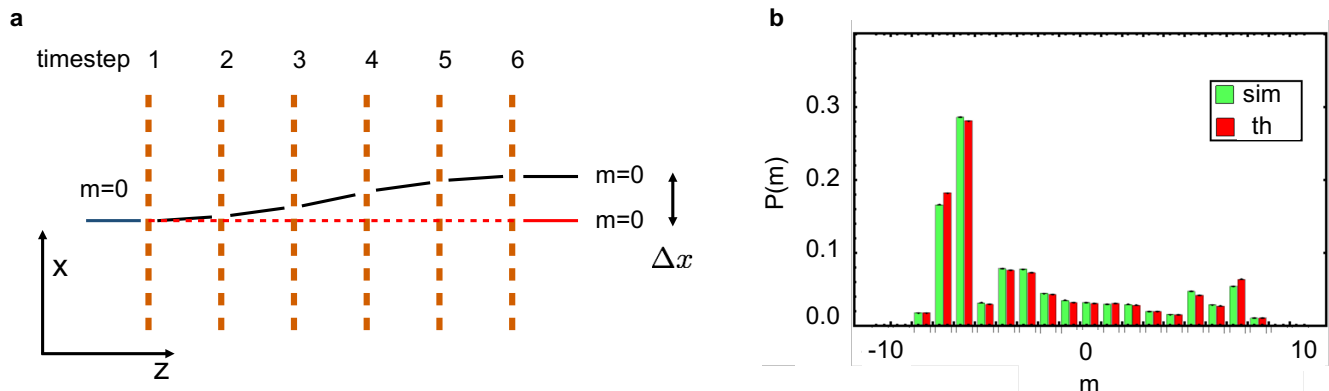
Supplementary Figure S7. **Group velocity detection**. Measurement of the y component of the group velocity $\mathbf{v}^{(+)}$, for the upper band of a QW with $\delta = \pi/2$. Each datapoint is obtained from a linear fit of the center of mass displacement of a Gaussian wavepacket.

Supplementary Note 7. POSSIBLE DEVIATIONS FROM THE IDEAL QW EVOLUTION

During propagation through the QW set-up, effects related to free space propagation of modes $|\mathbf{m}\rangle$ can act as perturbations to the ideal QW dynamics. In this section we describe the main phenomena that can take place in our



Supplementary Figure S8. **Wavepacket displacements for larger values of the force.** Band-averaged wavepacket displacements in the x and y directions, for $F = \pi/10$ (filled markers) and $F = \pi/5$ (empty markers), obtained combining measurements from the direct and inverse protocols, with $\delta = \pi/2$, for the lower band. Datapoints are experimental data, the continuous lines represent semi-classical predictions.



Supplementary Figure S9. **Deviations from the perfect simulation of a QW process.** **a**, At the input of the 1D QW we have a single beam with $\mathbf{k}_\perp = 0$, localized at the lattice site $m = 0$. At the exit of a 6-steps QW, we consider two contributions to the final wavefunction at site $m = 0$. One is resulting from the part of the input state that has been left unchanged (red). The second has gained Δk transverse momentum at the first three steps, and then has acquired opposite momentum at steps 4 to 6 (black). At the exit of the walk, also this component corresponds to the lattice site $m = 0$. However, the associated beams have some differences, which represent deviations from the ideal QW; being related to the same lattice site, they should be identical. First, they exit the walk laterally displaced by Δx , and the lack of overlap may reduce the interference, similarly to a decoherence effect. Second, the upper beam suffered a longer optical path, hence it accumulated a relative phase with respect to the central one. Finally, at each g -plate, the effective value of α_0 changes at each step for the deflected beam. **b**, Numerical simulation of a 1D walk with protocol $U = T_x W$, for $\delta = \pi/2$ and for an input state $|0, R\rangle$ (green columns), compared to a theoretical predictions of the ideal QW dynamics (red columns). After 10 steps differences are minimal.

system, and investigate their effect with the help of a numerical analysis. For simplicity, we will refer to a 1D QW, where modes $|\mathbf{m}\rangle$ are characterized by a single integer $m_x = m$.

There are essentially three “undesired” effects that may arise when considering the tilt in propagation direction *inside* the quantum walk:

1. At the end of the quantum walk, to each value of \mathbf{k}_\perp will correspond a superposition of waves that have followed different paths in the wavevector space, as illustrated in Supplementary Fig. S9a. These trajectories are actually associated with different optical paths. Associated relative phases are absent in the ideal QW dynamics and can modify the interference of the wavefunction components. To simulate this, the final amplitude of each mode $|\mathbf{m}\rangle$ can be calculated as the sum of all components related to these optical paths, multiplied by their relative

- phase. When propagating between two consecutive timesteps, mode $|0\rangle$ and a different mode $|s\rangle$ accumulate a phase delay $\Delta\phi_1 \approx (\pi\lambda ds^2)/(\Lambda^2)$, where d is the distance between consecutive steps.
2. The two beams considered in Supplementary Fig. S9a, that exit the walk in the same mode with $m = 0$, have an imperfect overlap that makes them partly distinguishable, since they are propagating along axes that are parallel but laterally displaced. These modes have a finite extension, and the absence of perfect spatial overlap results in a reduction of the interference visibility, similarly to a decoherence effect. Referring to the case presented above, between consecutive timesteps the two modes accumulate a lateral shift $|\Delta x| = d\lambda s/\Lambda$.
 3. A tilted beam hits two consecutive g -plates at points that have a relative shift. Eq. (3), describing the action of a g -plate, is derived by considering a Gaussian beam that hits the plate with its central position at $(x, y) = (0, 0)$. If the beam center is displaced by Δx , Eq. (3) remains valid after replacing α_0 with $\alpha'_0 = \alpha_0 + \Delta x \pi/\Lambda$, which represents the effective LC orientation at the beam central position. By looking at Eq. (3), we can observe that this effect results in additional phases accumulated by modes $|m\rangle$ during propagation, which have to be added to the phases associated with the different path lengths (see the previous point 1).

All these effects are estimated to be negligible for our setup. To make a quantitative check, in Supplementary Fig. S9b, we provide a comparison between an ideal QW evolution and the simulation of the real beam propagation through our set-up, by taking into account effects described in points (1-3) and using the real system parameters. After 10 steps of a 1D walk, we observe no significant deviations. This guarantees that also 5 steps of a 2D would not suffer any deviations. Indeed, such effects strongly depends on the typical order of the modes that are excited during the walk, which is of course limited by the highest possible order. In the first case, when starting from a localized input, the highest-order mode that can be excited has $|m| = \pm 10$. In the 2D case, highest-order excited modes have $|\mathbf{m}| = \sqrt{m_x^2 + m_y^2} = 5\sqrt{2} \approx 7$.

In prospect, when increasing the number of steps, we expect these systematic deviations from ideality to become progressively more relevant. On the other hand, if needed, these issues could be tackled by (i) changing the system parameters, in particular increasing Λ and reducing the step distance d , or (ii) by adopting a loop architecture combined with an imaging system. Indeed, by imaging the output of each step to the input of the following one, all the effects discussed above can be eliminated.